# Integrated FEM-Multibody Co-Simulation of Additively Manufactured Hip Prosthesis containing cracks

Roberto Di Bona, Domenico Gentile, Giuseppe Peter Vanoli
*University of Molise, Italy*
*roberto.dibona@unimol.it, domenico.gentile@unimol.it, giuseppe.vanoli@unimol.it*

Gabriel Testa, Sara Ricci
*University of Cassino and Southern Lazio, Italy*
*gabriel.testa@unicas.it, sara.ricci@unicas.it*

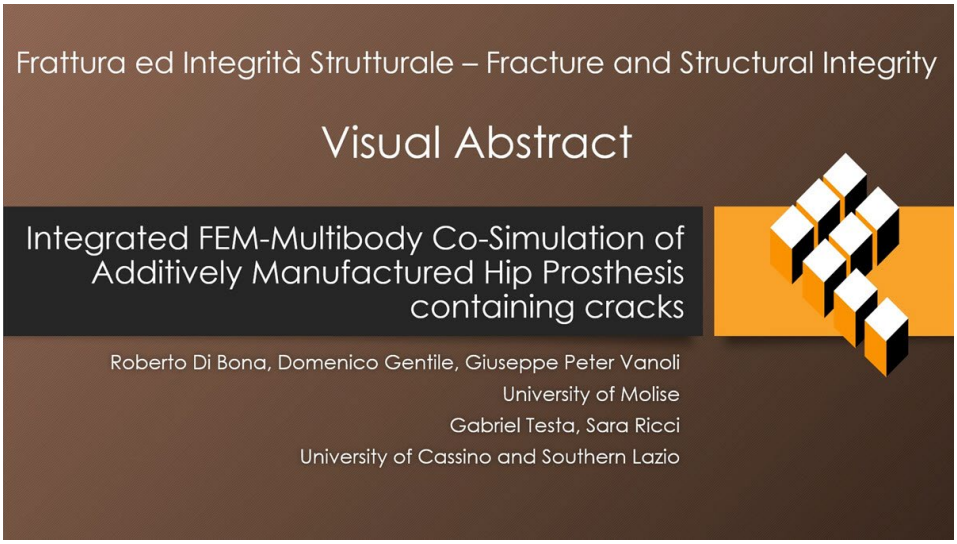


**Citation:** Di Bona, R., Gentile, D., Vanoli, G. P., Testa, G., Ricci, S., Integrated FEM-Multibody Co-Simulation of Additively Manufactured Hip Prosthesis containing cracks Fracture and Structural Integrity, 71 (2025) 108-123.

**Received:** 09.09.2024
**Accepted:** 11.10.2024
**Published:** 14.10.2024
**Issue:** 01.2025



**KEYWORDS.** Fracture mechanics, Co-simulation, Multi-body Dynamics, FEM, Additive manufacturing, Hip prosthesis

## INTRODUCTION

The Total Hip Arthroplasty (THA) is known to be one of the most common joint replacement surgeries. Due to advancements in biomedical technologies, the number of surgeries performed per year is steadily increasing, along with the tendency to operate on younger patients, instead of opting for less invasive, but seemingly less effective, techniques [8,23,24]. In the previous decade, numerous modular-type prostheses were designed, thanks to the ease of customizing a single design for the specific patient, as well as the advantages offered in the case of revision surgeries. However, the history of failures in ill-designed modular prostheses, along with the advancements in related medical and engineering technologies, highlights the promise of fabricating prostheses by 3D printing [8,26].

The complex mechanical nature of human tissues and biomechanics, coupled with the variation of body characteristics between different individuals, makes a technology capable of producing highly customized components particularly appealing. Advantages include the capability of mimicking the patients' extracellular matrix, increasing biocompatibility, and the ability to manufacture complex shapes that, coupled with the CAD reconstruction of human limbs from medical imaging techniques (such as Computed Tomography - CT and Magnetic Resonance Imagery - MRI), allow prosthesis design to be custom fit for the patient. However, there are still limitations such as the time needed to print the necessary scaffolding, and the stringent requirements for appropriate biocompatible materials, along with the extensive post-processing needed to ensure an acceptable product.

The Ti-6Al-4V alloy, also known as TC4 alloy, object of this work, is a popular choice in total hip replacements. Its advantages, compared to traditionally employed steel alloys, include high biocompatibility, resistance to corrosion in the quite aggressive body environment, density comparable to bone tissue, lower elastic modulus, while possessing good fatigue strength. Its main disadvantages are the poor shear behavior and wear resistance.

The use of additive manufacturing technology also allows to control the porosity of the component, so the elastic behavior can be adjusted to be similar of that of the human bone, which possesses a far lower elastic module than that of the TC4 alloy. This is shown to help reduce bone resorption in the patient and increase the service life of the prosthesis [32]. However, the microstructure and mechanical properties of AM materials can be extremely complex [6,16,30,34]. The properties of AM Ti6Al4V can exceed those of the conventional counterpart [13,29]. The work from Riemer & Richard [31] showed how appropriate heat treatments in additively manufactured hip prosthesis are essential in extending the component's life, even for the purpose of damage tolerant design. In TC4 alloys, the objective of the annealing heat treatment is to obtain a mixed alpha-beta microstructure from the starting alpha martensitic matrix of the as-built material. However, mistakes in the manufacturing process, such as wrong cooling rates, can lead to the nucleation of alpha phases in the beta phase grain boundaries, causing pitting and thus fatigue crack propagation [27].

The work of Molae & Fatemi [22] shows that, for additively manufactured TC4 alloys subject to multiaxial load, the failure mechanism and cracking behavior depend heavily on the microstructure, surface finish and the location of defects, ranging from Low Cycle Fatigue (LCF) to High Cycle Fatigue (HCF) and shear stress.

The subject of this paper is to provide a feasible method, employing the latest application of numerical analysis techniques, to analyze the structural behavior of a defective Ti6Al4V hip prosthesis, in order to correlate the propagation of defects to the premature failures experienced by patients, especially of young age and athletic disposition.

Hanusová et al. [11] dealt with the causes of failure for THA implants, and found that, while TC4 alloys present excellent fatigue behavior, manufacturing inaccuracies and micromotions located at the stem-neck interface, are the main causes for premature implant failure. It was demonstrated that the stress concentration caused crack growth, accelerated by the higher load experienced by the limb during demanding physical activities.

The possibility to foresee materials and structures' behavior in virtual environments is extremely appealing in the medical field to gain insight into failure mechanisms [18,33,35].

An MBD-FEM co-simulation was employed to investigate the crack propagation phenomenon, and to provide an example of the residual life estimation using Linear Elastic Fracture Mechanics (LEFM) related techniques.

## ANALYSIS PROCEDURE

The structural dynamics of a human femur subjected to Total Hip Arthroplasty (THA) during a simulated gait analysis was investigated by employing MSC Marc v2022, an implicit non-linear FEM commercial code. Implicit codes ensure higher stability and accuracy and are particularly well-suited for the static fracture analyses conducted in this study. Special attention was given to the meshing procedure to ensure an adequate representation of the femur's structural dynamics while avoiding excessive simulation complexity. Additionally, co-simulation analysis was performed using Adams v2022 and CoSim v2022. Adams will provide the Multi-Body Dynamics (MBD) simulation, while CoSim will facilitate the integration of Adams and Marc simulations, allowing for a comprehensive evaluation of the femur's response under the dynamic loading conditions of a simulated gait analysis. An MBD-FEM co-simulation allows for custom, tailor made simulation models, following the requirements in term of accuracy, performance and design optimization for the Industry 4.0 and 5.0 implementations.

The procedure employed in this work started from a previously developed [3] MBD model of an "android", performing a gait analysis, then the MBD-FEM co-simulation technology was implemented by coupling the android with a FEM model of a femur subject to THA. A gait analysis featuring the "healthy" prosthesis was performed, to act as reference, as shown in Figs. 1 and 2. Subsequently, two different series of defects were inserted in the hip prosthesis as cracks, in order to

evaluate the fatigue life of the defective component. The co-simulation architecture dictates the need for the coherence of measurement units between the MBD and FEM co-simulation files. For this reason, the results scalar, available in the Mentat and scPOST post-processors, relative to stresses are to be intended as kPa.

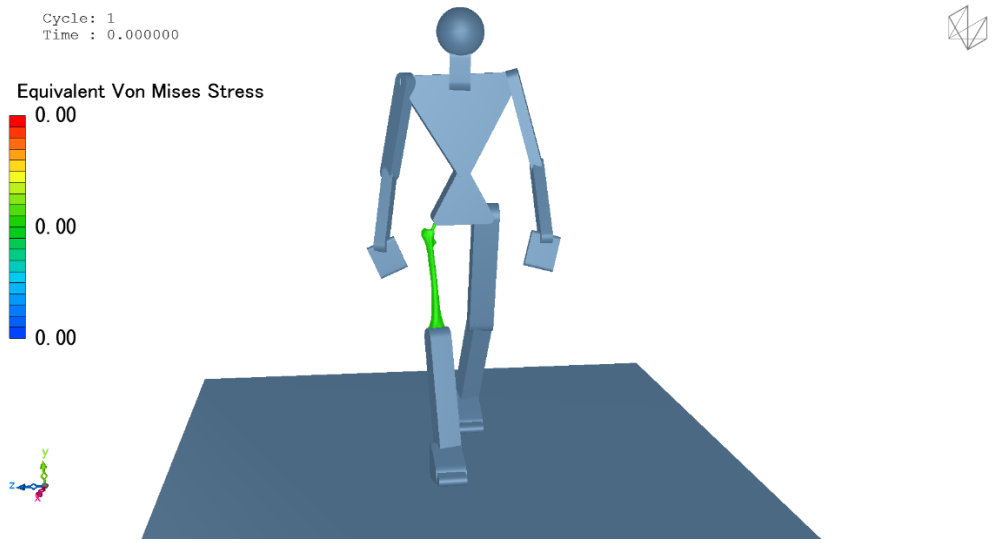


Figure 1: Co-Simulation post-processing at t=0s.

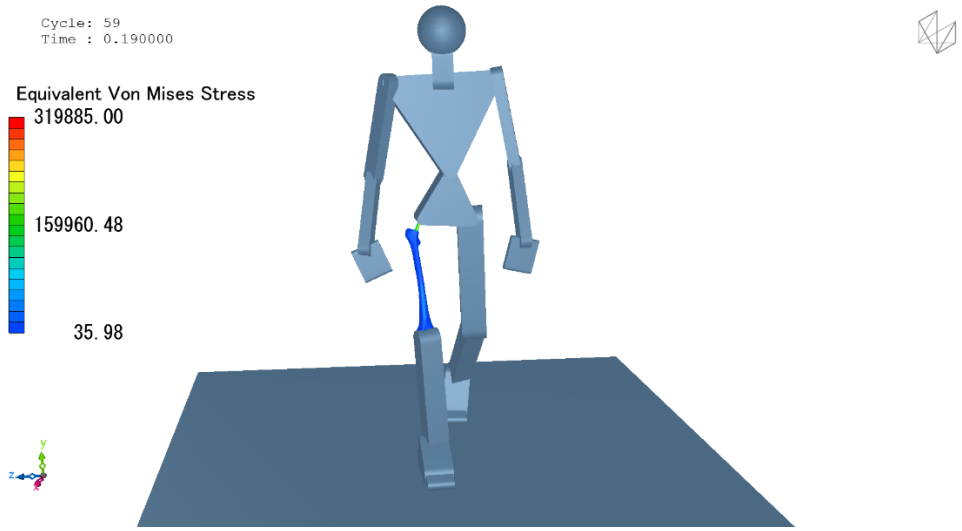


Figure 2: Co-Simulation post-processing at t=0.19s, where the Von Mises stress peak is reached.

### *Model definition*

The reference individual was an adult male 1.75m tall weighing 736N, as seen in [3]. The hip prosthesis employed is made up of two parts: the acetabulum, which is typically made of a metal alloy sphere incapsulated in a low friction material, and the actual prosthesis stem, made of metal alloy, that is inserted surgically in the femur. Fig. 3 shows a section view of the stem insertion in the femur in the FEM model.

The CAD model of the prosthesis was sourced from a thesis work [5]. The surgical acrylic cement was instead realized with an offset operation from the prosthesis stem. The actual configuration of the implants, including the amount and insertion method of the surgical cement, can vary depending on the specific patient and on the surgeon's judgment. The fundamental workflow for the prosthesis implantation in a simulated environment is described in [12]. In this case, the prosthesis was placed with its head's axis in a position compatible with the removed femur's head one. The three components were assembled through Boolean operations. The prosthesis' acetabulum was not modelled, as the purpose of this paper is not

to investigate the failures related to it. Instead, given the complexity of sourcing the necessary clinical data, it was assumed that its behavior can be approximated as an ideal spherical joint.

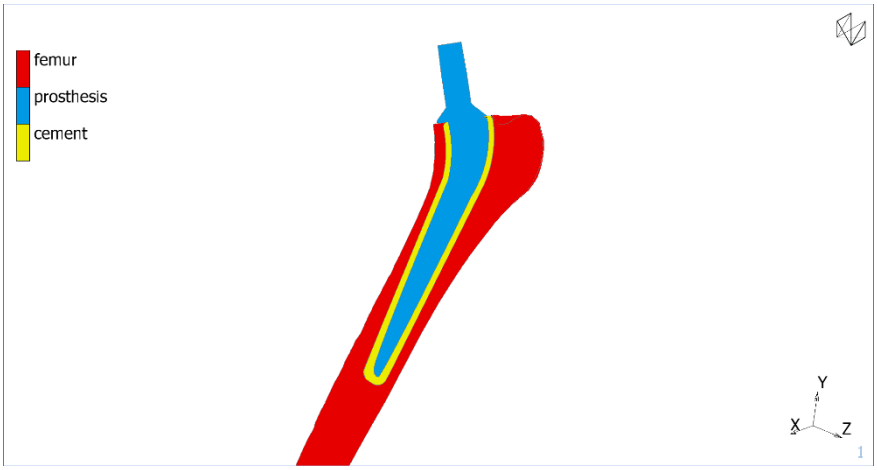


Figure 3: FEM model section.

Given the system's geometry, a full 3D analysis was performed.
The global coordinate system was modelled with the x-axis representing the positive direction of motion, as well as the body's sagittal axis, the y-axis as the longitudinal axis (upper direction positive) and the z-axis as the transverse axis (left-to-right direction positive).
The computational grid was created using the Patran volume automesher, with meshing parameters such as internal coarsening and curvature control to ensure an accurate representation of the complex geometrical features and the contact interfaces between different bodies, while still maintaining computational feasibility. 4-node tetrahedral elements with linear interpolation functions were employed.
The available literature [2,7,23] shows that the current procedure for testing implants using finite element analysis is to use static loads scaled to the patients' body weight. In this case, the boundary conditions for the FEM model, showed in Fig. 4, consist in a set of two nodes, placed at the same coordinates as the hip and knee joints in the MBD model, while linked, respectively, to the nodes of the prosthesis head and femur lower epiphysis. Through these nodes, the exchange of information between the MBD and FEM simulations, through the CoSim "glue" code, is realized, as shown in Fig. 5, and the boundary conditions for the model are supplied.

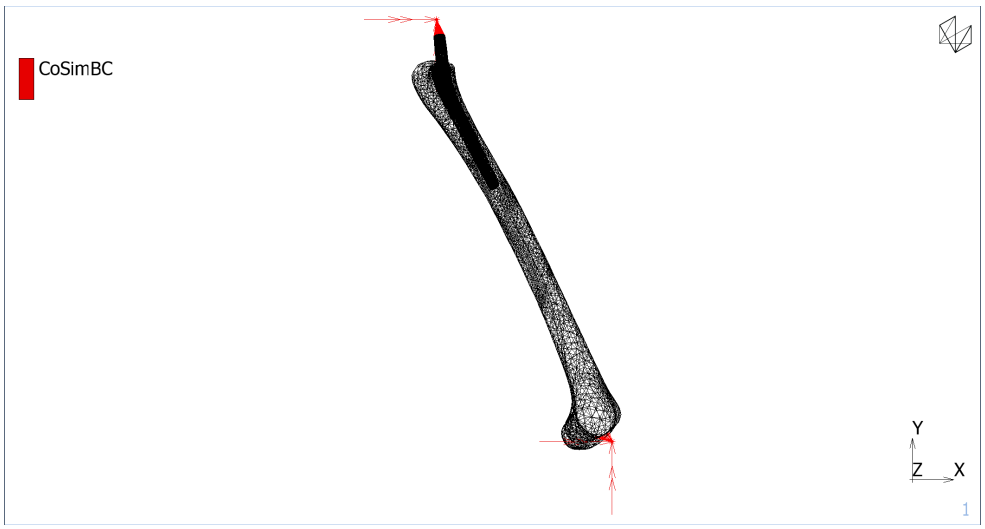


Figure 4: Boundary conditions for the FEM model.

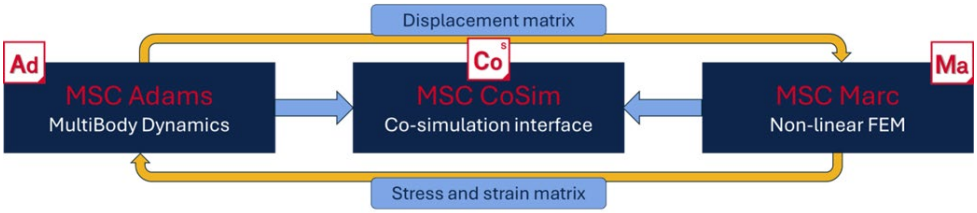


Figure 5: Co-simulation process scheme.

The advantage of using such a procedure lies in the possibility to evaluate with good accuracy the load history acting on the prosthesis, during a gait step, by taking into account the complete dynamics of the body, while retaining acceptable model complexity and simulation time.

### *Material properties*

Human bones are known to have a complex, strongly non-linear, mechanical behavior. For the purposes of the current study, the entire bone was modeled as cortical bone, as the focus is on the prosthesis, and the contribution of the trabecular bone sections is considered negligible. Therefore, an orthotropic linear elastic model was employed. The elastic constants, reported in Tab. 1, were sourced from [20,28].
To differentiate the behavior along the axial direction (y) and the two transverse directions (x and z), two different sets of parameters were employed.

| Characteristic | Value |
|---|---|
| Ex | 12.5 GPa |
| Ey | 18 GPa |
| Ez | 12.5 GPa |
| $\nu_{xy}$ | 0.36 |
| $\nu_{yz}$ | 0.36 |
| $\nu_{zx}$ | 0.4 |
| Gxy | 6.6 GPa |
| Gyz | 6.6 GPa |
| Gzx | 4.5 GPa |

Table 1: Bone elastic parameters [20,28].

The most common surgical cement employed is polymethylmethacrylate (PMMA), and its mechanical properties, including yield and ultimate tensile strength, are expected to be of average value. among the pool of data supplied by [25].
Ti6Al4V was chosen as the prosthesis material due to its extensive use and proven performance in medical applications [1,9].
Its yield and ultimate strength were evaluated according to the data used by [4], and are then assumed to be, respectively: 980MPa and 1000MPa.
Both the cement and the prosthesis were modelled with an isotropic elastic-perfectly plastic formulation, in order to reduce isolated nodal stress spikes resulting from contact interferences.
The implant of the prosthesis in the femur through the cement was modelled assuming a "glue" contact between the different parts, with a glue breakage stress assumed to be the cement's UTS, at 75MPa [25].

### *Crack parametrization*

Microstructural defects, related to the additive manufacturing process, are known to be favorable sites for crack initiation, whose propagation can be critical, resulting the failure of the prothesis [27].
The purpose of this study is to evaluate the SIF resulting from the crack application (in various configurations) in order to validate the model for predicting the evolution of damage in defective implants. Previous works on this subject [15,21] estimate a component life of several years, so, coupled with the modest load experienced by the average patient, it is unexpected to exceed the critical SIF ($K_{IC}$) of the prosthesis in a single cycle. More attention is then placed on the fatigue life of the component, meaning that the first objective of the study was to evaluate whether the SIF exceeds the threshold ($\Delta K_{th}$) for the linear regime in the Paris law. Then, more deep crack initiator surfaces were employed in order to obtain the range of $\Delta K_I$ and cycles to failure.

The Virtual Closure Crack Technique, embedded in Marc, was employed. It follows the description used in R.Krueger [17].

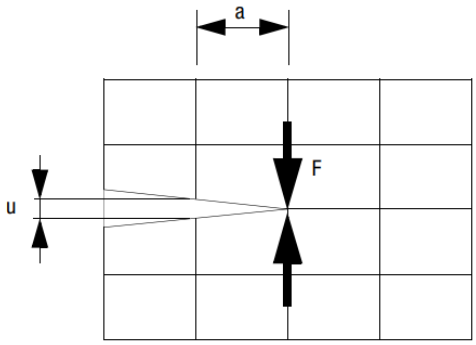


Figure 6: Virtual Closure Crack Technique reference geometry [17]

Considering the crack geometry as reported in Fig. 6, and having defined $G$ as the crack energy release rate, $\Pi$ as the energy release, $a$ as the defect size:

$$G = -\frac{\partial \Pi}{\partial a} \tag{1}$$

The total energy release rate is then computed as:

$$G_{tot} = G_I + G_{II} + G_{III} \tag{2}$$

Due to current limitations concerning the implementation of remeshing techniques in the co-simulation interface, the mechanisms of crack propagation were not investigated in the model. Instead, it was decided to estimate the crack growth by employing the standard Paris law, using the $\Delta K_I$ from the different crack geometries considered.
The Paris Law is featured as in Eqn. 3:

$$\frac{\partial a}{\partial N} = C\Delta K^m \tag{3}$$

where $a$ refers to the crack size; $N$ is the number of load cycles; $C$ and $m$ are material constants and $\Delta K$ is considered as the difference between the maximum and minimum SIF. Two additional parameters are considered: $\Delta K_{th}$ is the $\Delta K$ threshold value for the Paris law, and $K_{IC}$ refers to the fracture toughness.
The variability of crack growth parameters in Ti6Al4V was investigated in [4,14], in which the authors showed that the fabrication technique, subsequent heat treatments and crack growth direction relative to the build direction, play a significant role in crack initiation and propagation phenomena. This work refers to a selective laser melting (SLM) Ti6Al4V subject to an annealing heat treatment, performed at 890°C for two hours. The crack growth parameters are then referred to the specimens showing the fastest crack growth, and are reported as in Tab. 2:

| Parameter | Value [unit] |
|---|---|
| $\Delta K_{th}$ | 3.48 [MPa*m$^{0.5}$] |
| $K_{IC}$ | 53 [MPa*m$^{0.5}$] |
| C | 2.04*10$^{-12}$ [m/cycle] |
| m | 3.83 |

Table 2: Crack growth parameters [4,14].

*Procedure and results*

A preliminary co-simulation analysis without defects in the model, similar to the one performed in [3], was conducted, in order to estimate the critical sections for the bodies. The analysis consisted in a 1.24s long simulation of a single gait step, performed with the considered leg.

Predictably, the critical section of the prosthesis, in which the highest values of the Equivalent Von Mises Stress are found, is in proximity of the edge between the prosthesis head and stem, as shown in Fig. 7. The maximum value in this area is of 319.8MPa, which is lower than the yield stress for the Ti6Al4V. However, considering that crack propagation is governed by the maximum principal stress, it is important to evaluate how this quantity is distributed in the model. This is observed on the opposite side of the prosthesis, reaching a maximum value of 270MPa, as shown in Figs. 8 and 9.
By examining the reaction forces acting on the boundary condition nodes, it was possible to confirm the multiaxial nature of the load experienced by the prosthesis. For this purpose, the force components are expressed along the global reference system, while the moment components act around the same axes. For t=0.19s, it was evident that the most influent component was the moment resulting from the femur bending movement ($M_z$), followed by the vertical component of the force ($F_y$), caused by the body weight.
The total magnitude of the forces, labelled Joint Reaction Force according to the procedure used by [23], was calculated as:

$$JRF = \sqrt{F_x^2 + F_y^2 + F_z^2} \tag{4}$$

It was useful to also evaluate a Joint Reaction Moment, as:

$$JRM = \sqrt{M_x^2 + M_y^2 + M_z^2} \tag{5}$$

The resulting values, for the time increment here considered, amount respectively to 710.1N and 34.55Nm. The existing literature estimates the force peak during gait to be about 3 times the body weight [23], but in the case of this simulation the load was shown to be largely due to the bending moment.

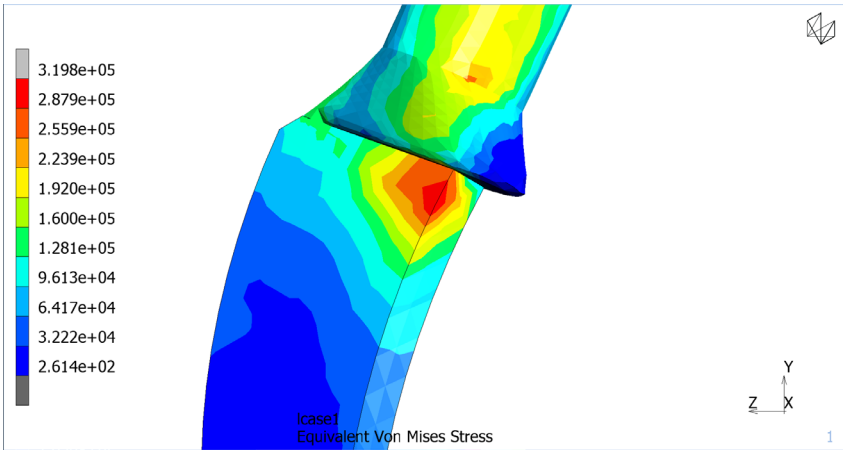


Figure 7: Equivalent VM stress distribution on prosthesis in preliminary analysis at t=0.19s.

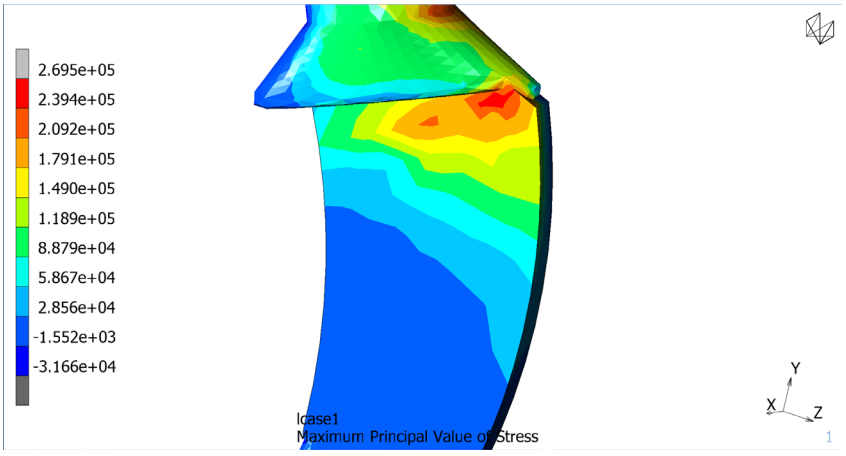


Figure 8: Maximum principal value of stress distribution on prosthesis in preliminary analysis at t=0.19s.

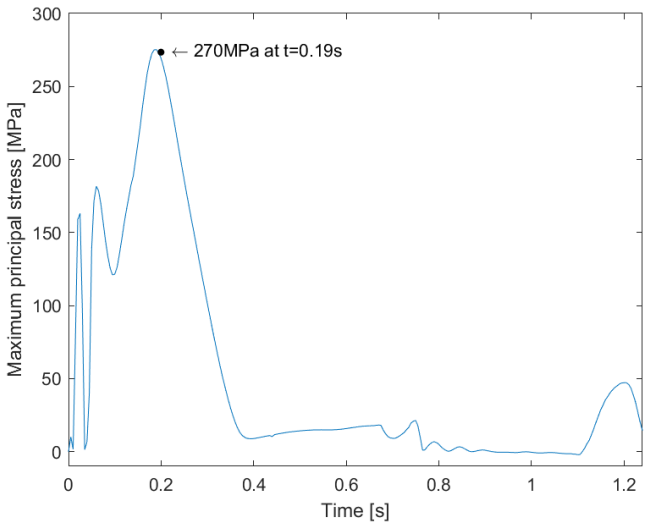


Figure 9: Maximum principal value of stress history on most loaded node in preliminary analysis.

Once the healthy model reference was obtained, the LEFM analyses were performed. The cracks are chosen to be surfacing, in order to consider the most critical situation, featuring the highest $K_I$ for the specific configuration. The crack orientation follows the maximum principal stress vector at the crack tip coordinates in the initial, uncracked model. This approximation is due to the current limitations in employing remeshing techniques in a co-simulation.

In the first set of analyses (here called Case 1X, with X being A B or C depending on the ascending crack size), the cracks were initiated, by remeshing the model through the use of a set of three cutting planes, passing through the section of the prosthesis exhibiting the maximum Equivalent Von Mises Stress, with increasing depth. (Figs. 10, 11, 12, 13, 14, 15). This was done in order to obtain a series of $\Delta K_I$ values, to estimate the propagation speed and the component residual life. The crack tip area exhibited an average element size ranging from 0.2 to 0.5mm. The starting crack size was considered to be the first showing a maximum $K_I$ value higher than the threshold, the final crack size was the maximum size allowed before resulting in the component plastic failure from the lack of a resistant section. This is highlighted by the presence of plastic strain areas at the crack tip, as shown in Fig. 16.

A second series of analyses was performed, by also considering three increasing crack depths, called Case 2 (Figs. 17, 18, 19, 20, 21, 22). A particularly critical situation was evaluated, where the starting crack tip reaches the node featuring the maximum principal stress value in the preliminary analysis, with the final crack causing the component failure in the following cycle. The $\Delta K_I$ history for Case 2 is shown in Fig. 23.

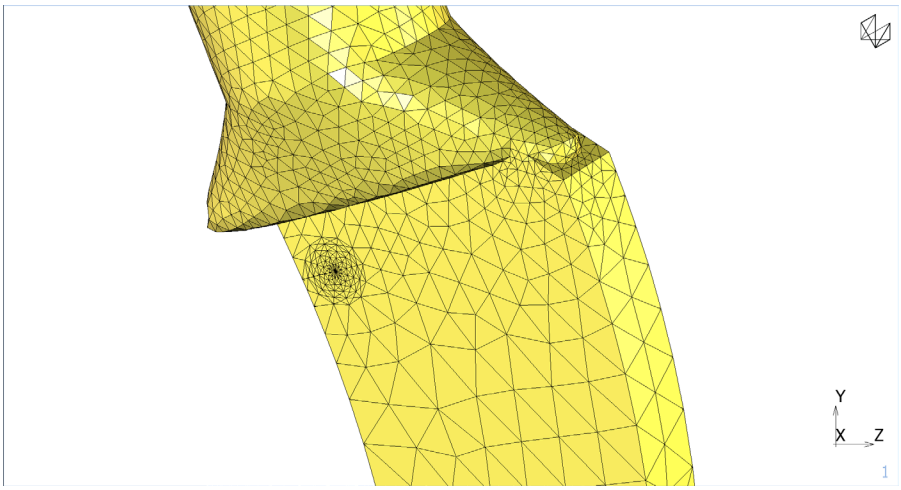


Figure 10: Case 1A mesh (crack depth: 2.1mm).

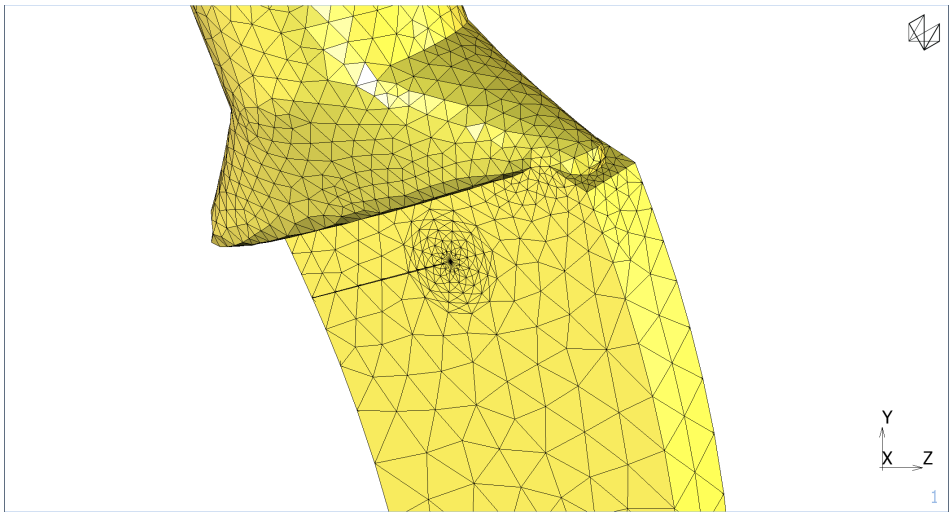


Figure 11: Case 1B mesh (crack depth: 8.3mm).

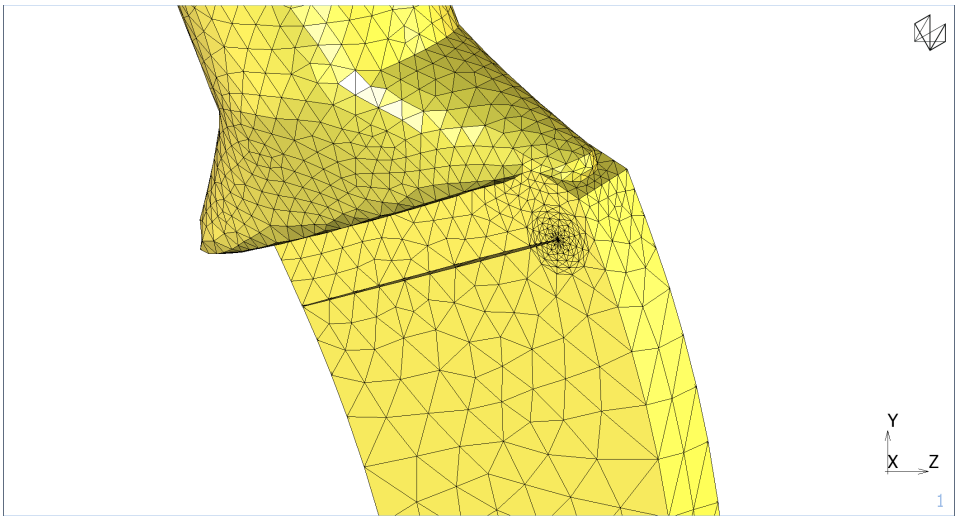


Figure 12: Case 1C mesh (crack depth: 15.5mm).

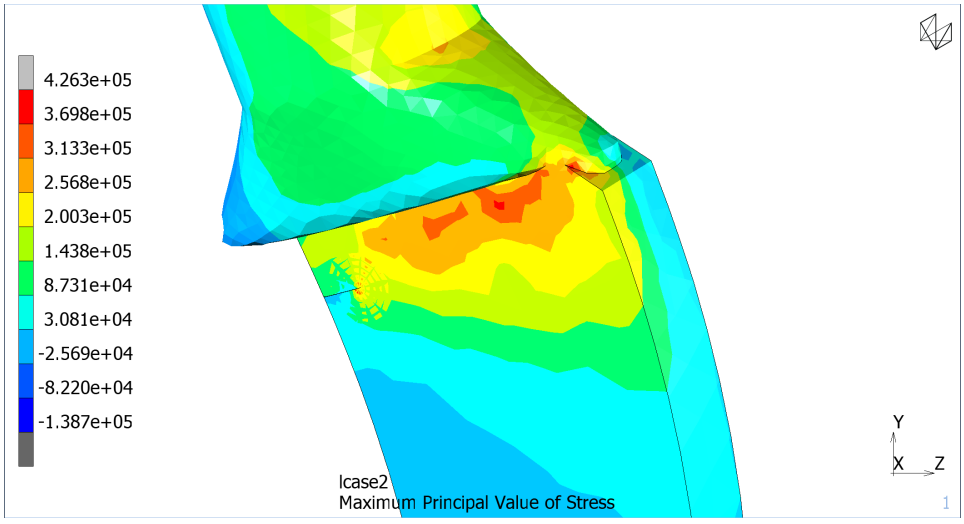


Figure 13: Case 1A Maximum principal value of stress distribution at t=0.19s.

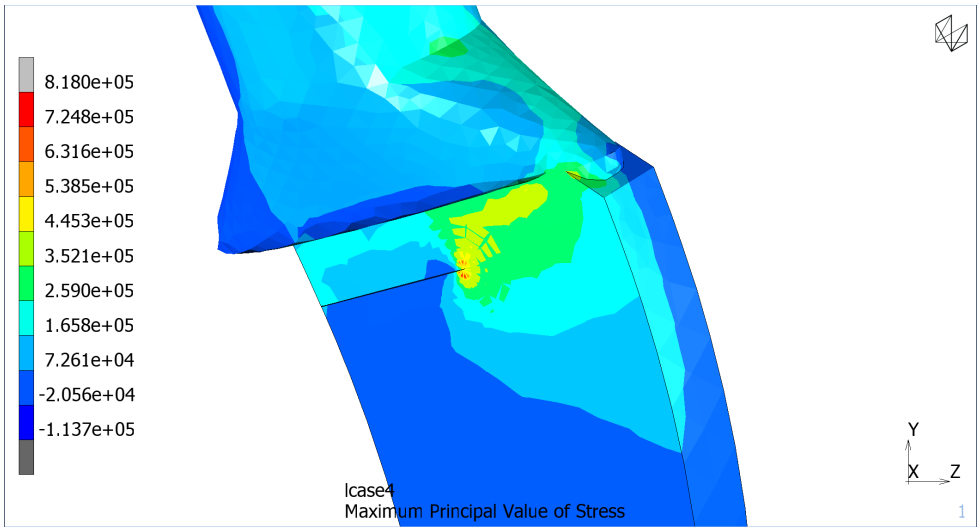


Figure 14: Case 1B Maximum principal value of stress distribution at t=0.19s.

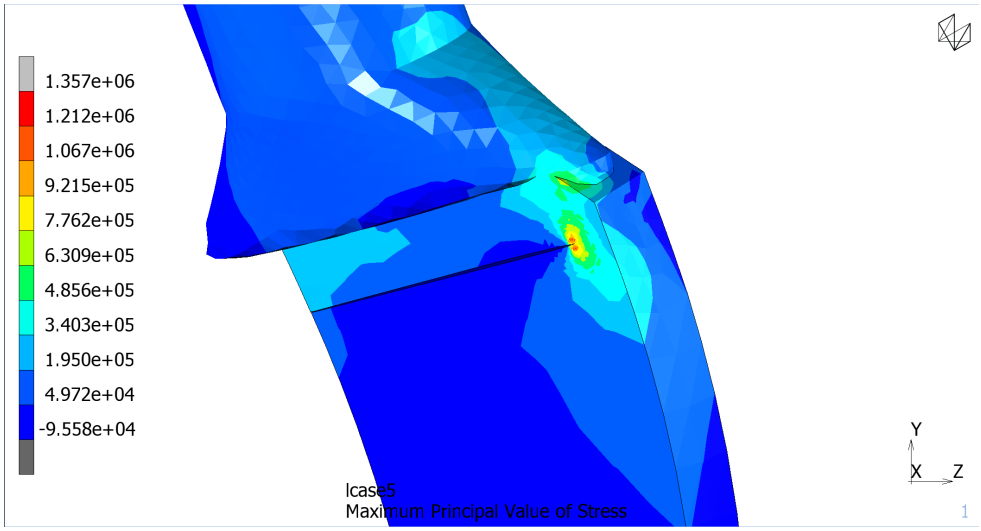


Figure 15: Case 1C Maximum principal value of stress distribution at t=0.19s.

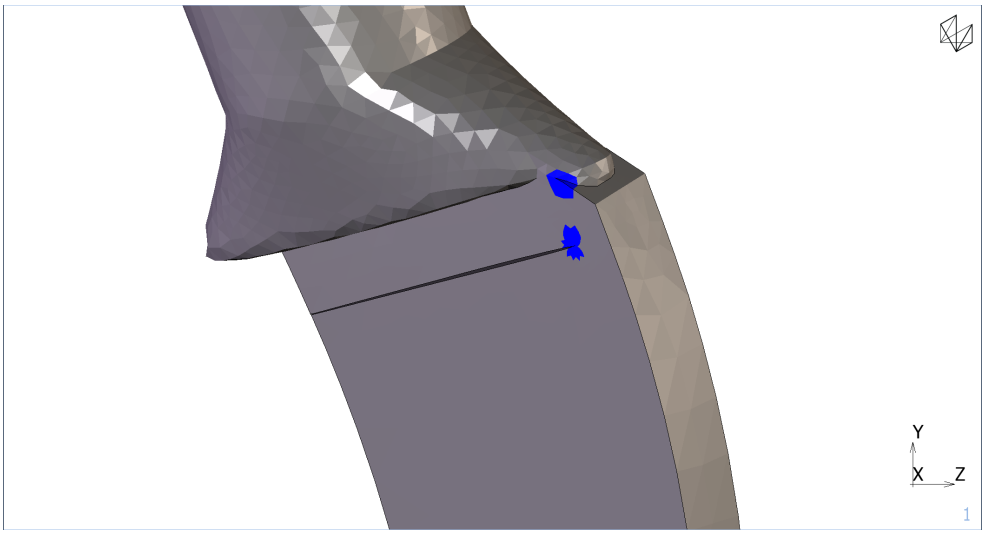


Figure 16: Plastic strain areas (in blue) for Case 1C.

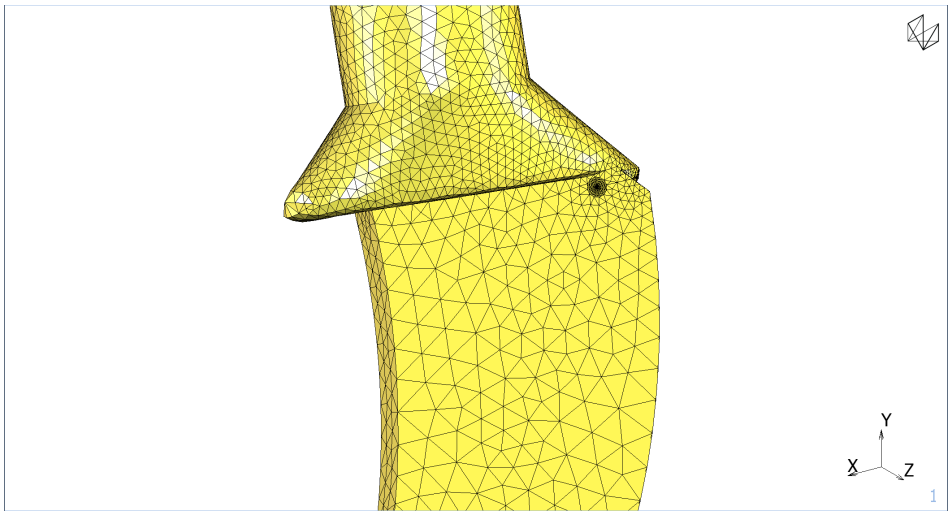


Figure 17: Case 2A mesh (crack depth: 2.6mm).

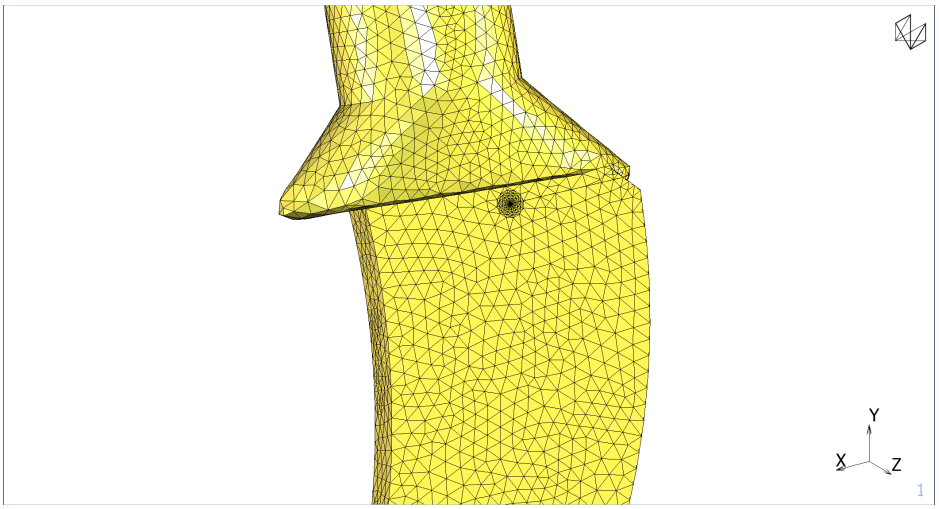


Figure 18: Case 2B mesh (crack depth: 8mm).

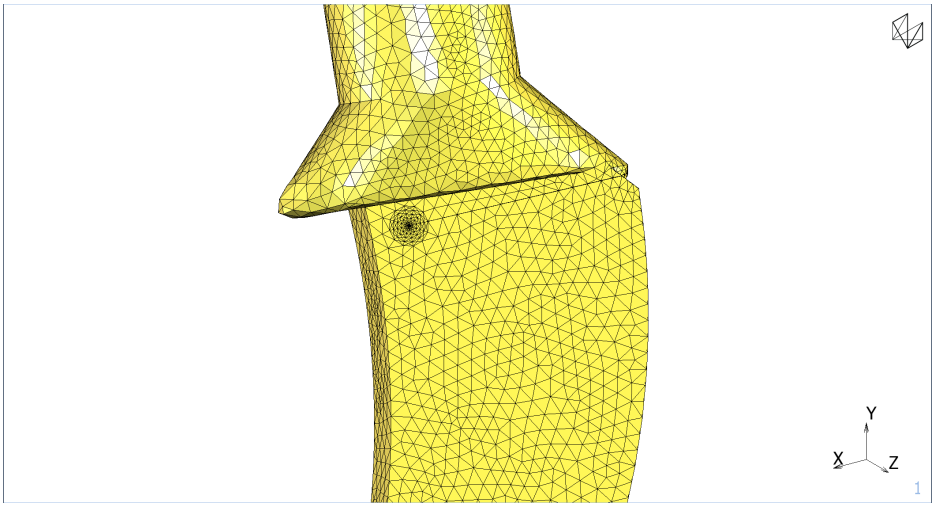


Figure 19: Case 2C mesh (crack depth: 14.3mm).

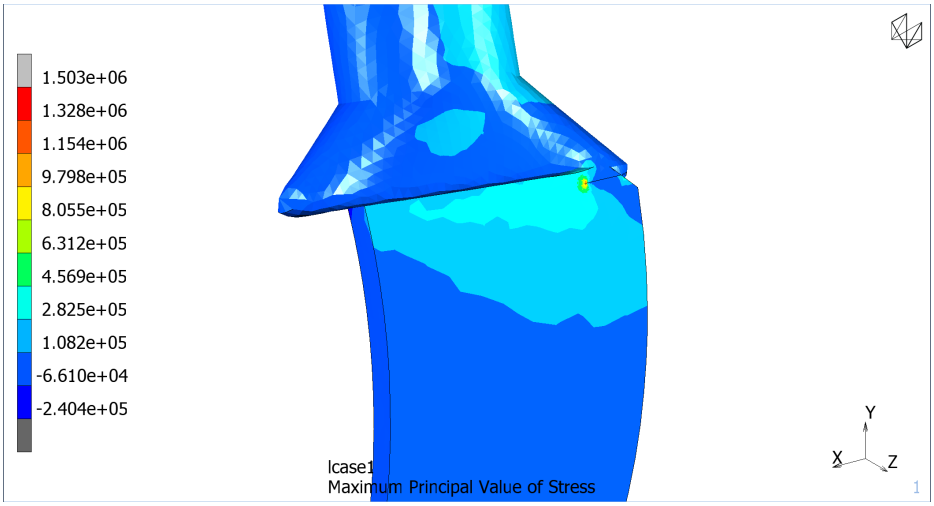


Figure 20: Case 2A Maximum principal value of stress distribution at t=0.19s.

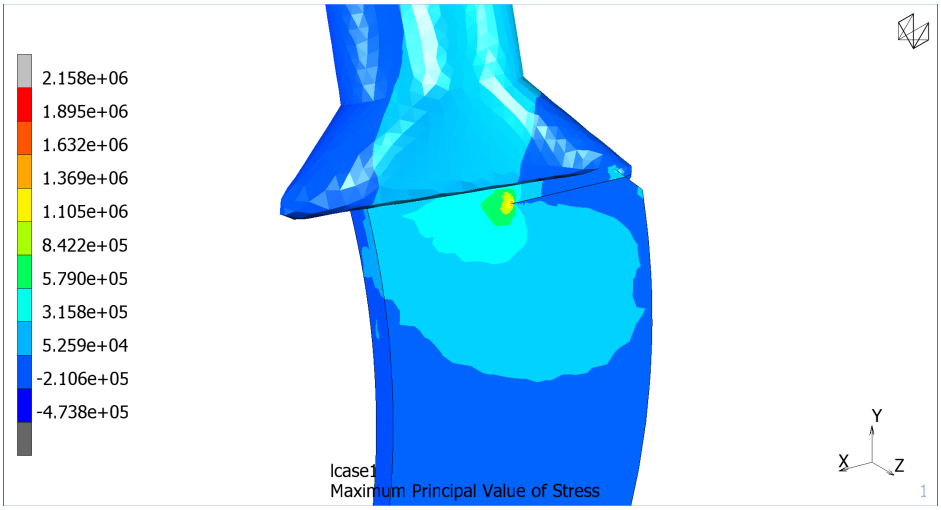


Figure 21: Case 2B Maximum principal value of stress distribution at t=0.19s.

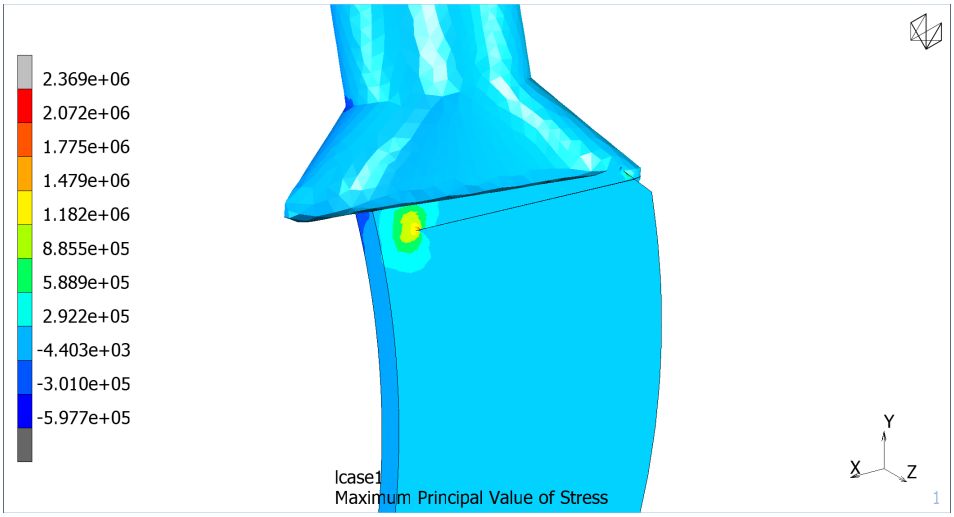


Figure 22: Case 2C Maximum principal value of stress distribution at t=0.19s.

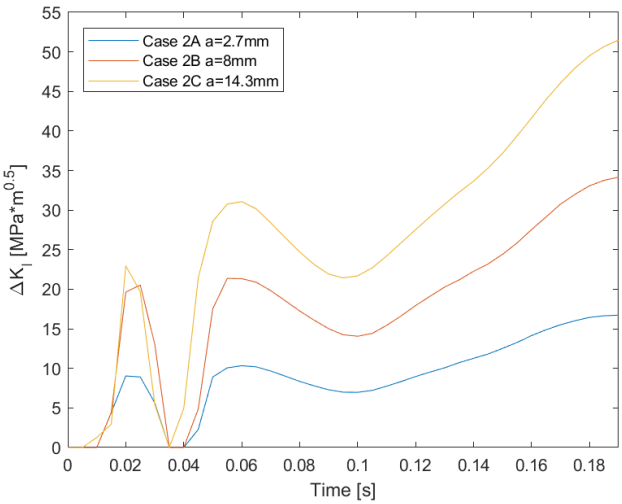


Figure 23: Case 2 $\Delta K_I$ history.

The results are then compared between the two cases, as shown in Tab. 3. Considering Case 1, while the crack tips exhibit a noticeable stress concentration, according to the expected lobe shaped distribution from the tip, the $\Delta K_I$ in Case 1C does not reach the $K_{IC}$ value for the material. Instead, as shown in Fig. 16, the component fails by exceeding the yield value for the material and developing a noticeable plastic zone, due to the lack of sufficient resistant section.

While considering the Case 2 series of simulations, it is evident that both the stress and the $\Delta K_I$ show higher values, as the crack was initiated through the section showing the highest principal value of stress, which is known to be the cause for crack nucleation and propagation. This is further exemplified in Figs. 24 and 25, where the two variables of interest's growth is plotted, for the two cases, against the crack depth increase. Fig. 26 provides the plot of the Paris law, in the specific interval, for the two cases.

| Case 1 | Crack depth [mm] | Maximum principal value of Stress [MPa] | $\Delta K_I$ [MPa*m$^{0.5}$] | Case 2 | Crack depth [mm] | Maximum principal value of Stress [MPa] | $\Delta K_I$ [MPa*m$^{0.5}$] |
|---|---|---|---|---|---|---|---|
| 1A | 2.1 | 426 | 3.8 | 2A | 2.6 | 1503 | 16.6 |
| 1B | 8.3 | 818 | 16.1 | 2B | 8 | 2158 | 34.3 |
| 1C | 15.5 | 1357 | 32.5 | 2C | 14.3 | 2369 | 51.5 |

Table 3: Result scalar comparison between cases.

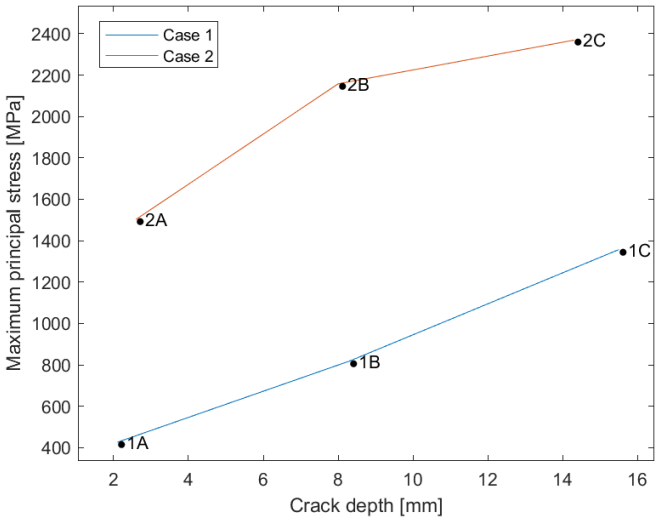


Figure 24: Maximum principal stress increase with crack growth in the two cases.

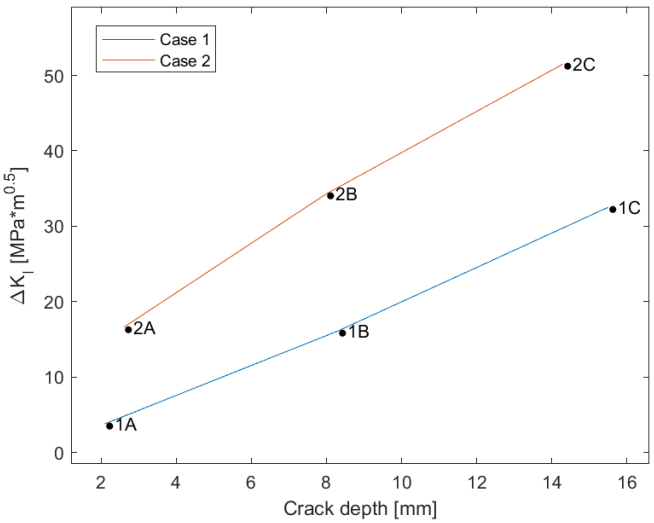


Figure 25: $\Delta K_I$ increase with crack growth in the two cases.

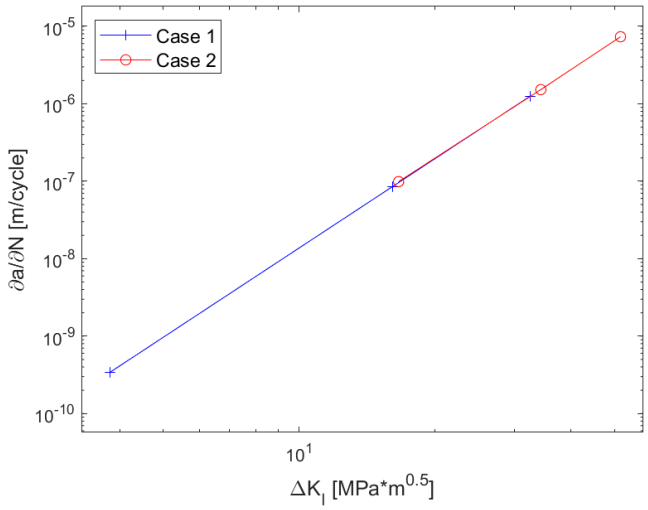


Figure 26: $\Delta K_I$ versus $\partial a/\partial N$ for the two cases.

The Paris Law is then applied to estimate the cycles to fracture, in the two cases, as shown in Tab. 4:

| Case 1 | Crack growth [mm] | Cycles | Case 2 | Crack growth [mm] | Cycles |
|---|---|---|---|---|---|
| 1A to 1B | 6.2 | $1.3*10^7$ | 2A to 2B | 5.4 | $5.5*10^4$ |
| 1B to 1C | 7.2 | $8.3*10^4$ | 2B to 2C | 6.3 | $4.1*10^3$ |
| Cumulated | 13.4 | $1.3*10^7$ | Cumulated | 11.7 | $5.9*10^4$ |

Table 4: Residual life estimation through LEFM in the two cases.

As expected, the crack growth in Case 1 is considerably slow, and is not endangering the life of the prosthesis. Instead, the Case 2 shows a residual life of about 59000 cycles, placing it on the lower end of HCF as failure mode. As reported by [19], the average elderly person, who is the principal recipient for THA operations, walks an average of 2700 to 7500 steps per day. This results in a component life of merely 7 to 21 days and is far lower than the number of cycles a functional prosthesis is required to experience [10].

## CONCLUSIONS

The MBD-FEM co-simulation technique was employed to examine the innovative case of a gait analysis coupled with a fracture mechanics analysis of a defective THA. The stress distribution and fatigue life of the component, subject to realistic loads sourced from the MBD analysis, were evaluated, allowing to find the most critical configuration for the crack, and to reach the conclusion that cracks occurring on a 3D-printed hip prosthesis, resulting from a defective manufacturing process, can critically endanger the reliability of the implant, potentially causing injuries and requiring additional surgical treatments. Even with the current study limitations, the CAE tools are then proved to be of assistance in the analysis of the most pressing issues in the biomechanical engineering field. Further studies can stem from this work.

## ACKNOWLEDGEMENTS

The authors acknowledge support and funding for this work from the MolisCTE Verticale II, NICE project.

## REFERENCES

[1] Aghili, S.A., Hassani, K., Nikkhoo, M. (2021). A finite element study of fatigue load effects on total hip joint prosthesis, Comput Methods Biomech Biomed Engin, 24(14), pp. 1545–1551. DOI: 10.1080/10255842.2021.1900133.

[2] Babić, M., Verić, O., Božić, Ž., Sušić, A. (2020). Finite element modelling and fatigue life assessment of a cemented total hip prosthesis based on 3D scanning, Eng Fail Anal, 113, p. 104536. DOI: 10.1016/j.engfailanal.2020.104536.

[3] Di Bona, R., Catelani, D., Ottaviano, E., Gentile, D., Testa, G. (2024). MB and Non-Linear FEM Co-Simulation Techniques for the Biomechanics of the Human Body with Hip Prosthesis (IN REVIEW), Multibody Syst Dyn. DOI: 10.21203/rs.3.rs-4821460/v1.

[4] Cain, V., Thijs, L., Van Humbeeck, J., Van Hooreweder, B., Knutsen, R. (2015). Crack propagation and fracture toughness of Ti6Al4V alloy produced by selective laser melting, Addit Manuf, 5, pp. 68–76. DOI: 10.1016/j.addma.2014.12.006.

[5] Cirnelli, S. (2023). FEM Analysis of the Propagation of a Defect in the Titanium Alloy Femur Stem of a Hip Prosthesis. University Of Molise.

[6] Cognigni, F., Sgambetterra, M., Zucca, G., Gentile, D., Ricci, S., Testa, G., Rizzi, G., Rossi, M. (2023). Multimodal and multiscale investigation for the optimization of AlSi10Mg components made by powder bed fusion-laser beam, Discov Mater, 3(1), p. 21. DOI: 10.1007/s43939-023-00058-2.

[7] Colic, K., Sedmak, A. (2016). The current approach to research and design of the artificial hip prosthesis: a review, Rheumatology and Orthopedic Medicine, 1(1). DOI: 10.15761/ROM.1000106.

[8] Fang, S., Wang, Y., Xu, P., Zhu, J., Liu, J., Li, H., Sun, X. (2022). Three-dimensional-printed titanium implants for severe acetabular bone defects in revision hip arthroplasty: short- and mid-term results, Int Orthop, 46(6), pp. 1289–1297. DOI: 10.1007/s00264-022-05390-5.

[9] Felli, F., Pilone, D., Scicutelli, A. (2016). Fatigue behaviour of titanium dental endosseous implants, Frattura Ed Integrità Strutturale, 5(18), pp. 14–22. DOI: 10.3221/IGF-ESIS.18.02.

[10] Griza, S., Zanon, G., Silva, E.P., Bertoni, F., Reguly, A., Strohaecker, T.R. (2009). Design aspects involved in a cemented THA stem failure case, Eng Fail Anal, 16(1), pp. 512–520. DOI: 10.1016/J.ENGFAILANAL.2008.06.016.

[11] Hanusová, P., Palček, P., Uhríčik, M. (2019). Analysis of the cause of titanium endoprosthesis failure, Manufacturing Technology, 19(5), pp. 749–752. DOI: 10.21062/UJEP/366.2019/A/1213-2489/MT/19/5/749.

[12] https://www.materialise.com/en/inspiration/cases/automating-key-components-of-finite-element-research. (n.d.).

[13] Iannitti, G., Bonora, N., Testa, G., Ruggiero, A. (2021). High-rate characterization of additively manufactured Ti-6Al-4V using Taylor cylinder impact test: Experiments, Material Design & Processing Communications, 3(5). DOI: 10.1002/mdp2.192.

[14] Jones, R., Michopoulos, J.G., Iliopoulos, A.P., Singh Raman, R.K., Phan, N., Nguyen, T. (2018). Representing crack growth in additively manufactured Ti-6Al-4V, Int J Fatigue, 116, pp. 610–622. DOI: 10.1016/j.ijfatigue.2018.07.019.

[15] Kiani Khouzani, M., Bahrami, A., Eslami, A. (2018). Metallurgical aspects of failure in a broken femoral HIP prosthesis, Eng Fail Anal, 90, pp. 168–178. DOI: 10.1016/J.ENGFAILANAL.2018.03.018.

[16] Konecná, R., Kunz, L., Nicoletto, G., Baca, A. (2015). Fatigue crack growth behavior of Inconel 718 produced by selective laser melting, Frattura Ed Integrità Strutturale, 10(35), pp. 31–40. DOI: 10.3221/IGF-ESIS.35.04.
[17] Krueger, R. (2004). Virtual crack closure technique: History, approach, and applications, Appl Mech Rev, 57(2), pp. 109–143. DOI: 10.1115/1.1595677.
[18] Kytyr, D., Doktor, T., Jirousek, O., Zlamal, P., Pokorny, D. (2010). Experimental and numerical study of cemented bone-implant interface behavior, Frattura Ed Integrità Strutturale, 5(15), pp. 5–13. DOI: 10.3221/IGF-ESIS.15.01.
[19] Lee, I.-M., Shiroma, E.J., Kamada, M., Bassett, D.R., Matthews, C.E., Buring, J.E. (2019). Association of Step Volume and Intensity With All-Cause Mortality in Older Women, JAMA Intern Med, 179(8), p. 1105. DOI: 10.1001/jamainternmed.2019.0899.
[20] Mirzaali, M.J., Schwiedrzik, J.J., Thaiwichai, S., Best, J.P., Michler, J., Zysset, P.K., Wolfram, U. (2016). Mechanical properties of cortical bone and their relationships with age, gender, composition and microindentation properties in the elderly, Bone, 93, pp. 196–211. DOI: 10.1016/J.BONE.2015.11.018.
[21] Modi, S.R., Jha, K. (2023). Multi-mode fracture analysis for critical crack size and life estimation of hip prosthesis using extended finite element method, Journal of Mechanical Science and Technology, 37(2), pp. 1047–1053. DOI: 10.1007/s12206-023-0143-0.
[22] Molaei, R., Fatemi, A. (2019). Crack paths in additive manufactured metallic materials subjected to multiaxial cyclic loads including surface roughness, HIP, and notch effects, Int J Fatigue, 124, pp. 558–570. DOI: 10.1016/J.IJFATIGUE.2019.03.007.
[23] Okolie, O., Stachurek, I., Kandasubramanian, B., Njuguna, J. (2021). Material Challenges and Opportunities in 3D Printing for Hip Implant Applications, Recent Prog Mater, 4(1), pp. 1–1. DOI: 10.21926/rpm.2201004.
[24] Okolie, O., Stachurek, I., Kandasubramanian, B., Njuguna, J. (2020). 3D Printing for Hip Implant Applications: A Review, Polymers (Basel), 12(11), p. 2682. DOI: 10.3390/polym12112682.
[25] Overview of materials for Acrylic, Cast. (n.d.). Available at: https://www.matweb.com/search/DataSheet.aspx?MatGUID=a5e93a1f1fff43bcbac5b6ca51b8981f.
[26] Park, J.-W., Kang, H.-G., Kim, J.-H., Kim, H.-S. (2021). 3D-Printed Connector for Revision Limb Salvage Surgery in Long Bones Previously Using Customized Implants, Metals (Basel), 11(5), p. 707. DOI: 10.3390/met11050707.
[27] Pimenta, A.R., Tavares, S.S.M., Dias, D.F., Correa, S.R., Sobreiro, A.L., Diniz, M.G. (2021). Failure Analysis of a Titanium Hip Prosthesis, Journal of Failure Analysis and Prevention, 21(1), pp. 28–35. DOI: 10.1007/s11668-020-01041-2.
[28] Reilly, D.T., Burstein, A.H. (1975). The elastic and ultimate properties of compact bone tissue, J Biomech, 8(6), pp. 393–405. DOI: 10.1016/0021-9290(75)90075-5.
[29] Ricci, S., Iannitti, G. (2024). Mechanical Behavior of Additive Manufacturing (AM) and Wrought Ti6Al4V with a Martensitic Microstructure, Metals (Basel), 14(9), p. 1028. DOI: 10.3390/met14091028.
[30] Ricci, S., Zucca, G., Iannitti, G., Ruggiero, A., Sgambetterra, M., Rizzi, G., Bonora, N., Testa, G. (2023). Characterization of Asymmetric and Anisotropic Plastic Flow of L-PBF AlSi10Mg, Exp Mech, 63(8), pp. 1409–1425. DOI: 10.1007/s11340-023-00995-2.
[31] Riemer, A., Richard, H.A. (2016). Crack Propagation in Additive Manufactured Materials and Structures, Procedia Structural Integrity, 2, pp. 1229–1236. DOI: 10.1016/J.PROSTR.2016.06.157.
[32] Risse, L., Woodcock, S., Brüggemann, J.P., Kullmer, G., Richard, H.A. (2022). Stiffness optimization and reliable design of a hip implant by using the potential of additive manufacturing processes, Biomed Eng Online, 21(1), pp. 1–13. DOI: 10.1186/S12938-022-00990-Z/FIGURES/6.
[33] Sedmak, A., Čolić, K., Grbović, A., Balać, I., Burzić, M. (2019). Numerical analysis of fatigue crack growth of hip implant, Eng Fract Mech, 216, p. 106492. DOI: 10.1016/j.engfracmech.2019.106492.
[34] Wang, L. (2022). Microstructure and anisotropic tensile performance of 316L stainless steel manufactured by selective laser melting, Frattura Ed Integrità Strutturale, 16(60), pp. 380–391. DOI: 10.3221/IGF-ESIS.60.26.
[35] Zengah, S., Mankour, A., Abderahmane, S., Salah, H., Mallek, A., Bouziane, M.M. (2022). Numerical Analysis of the Crack Growth Path in the Cement of Hip Spacers, Frattura Ed Integrità Strutturale, 16(61), pp. 266–281. DOI: 10.3221/IGF-ESIS.61.18.